Ching-Tai Ng, Hasan Mohseni, Heung-Fai Lam
Debonding detection in CFRP-retrofitted reinforced concrete structures using nonlinear Rayleigh wave
Mechanical Systems and Signal Processing, 2018; 125:245-256

Final publication at http://dx.doi.org/10.1016/j.ymssp.2018.08.027

Debonding Detection in CFRP-retrofitted Reinforced Concrete Structures using Nonlinear Rayleigh Wave

Ching-Tai Ng[1,*], Hasan Mohseni[1], Heung-Fai Lam[2]

[1] School of Civil, Environmental & Mining Engineering, The University of Adelaide, 5005 SA, Australia

[2] Department of Architecture and Civil Engineering, City University of Hong Kong, Hong Kong, P.R., China

Abstract

This paper proposed to use nonlinear Rayleigh wave to inspect debonding in carbon fibre reinforced polymer (CFRP) retrofitted reinforced concrete structures. The proposed method requires a network of transducers that are used to sequentially scan the CFRP-retrofitted reinforced concrete structures by transmitting and receiving Rayleigh wave. The nonlinear feature used for the debonding detection is second harmonic generation due to the interaction of Rayleigh wave at the debonding between the CFRP and concrete interfaces. A damage image reconstruction algorithm is proposed to provide a graphical representation for detecting and locating the debonding in the CFRP-retrofitted reinforced concrete structures. In this study, experimental case studies are used to demonstrate the performance of the proposed debonding detection technique. A transducer network with four piezoelectric transducers is used to actuate Rayleigh wave and measure the second harmonic wave in the experiments. The results show that the proposed debonding detection technique is reliable in detecting and locating the debonding in the CFRP-retrofitted reinforced concrete structures.

Keywords: Nonlinear Rayleigh wave; higher harmonic; debonding; CFRP-retrofitted reinforced concrete; damage detection; contact nonlinearity

---

[*] Corresponding author: alex.ng@adelaide.edu.au

Introduction

Ensuring structural integrity and safety is of paramount importance for a wide range of engineering structures as evidenced by extensive research work on developing damage detection techniques [1]-[4]. In the literature, different damage detection techniques were developed [4]-[7]. Among these developments, guided waves have been widely recognised as one of the promising damage detection approaches. Guided waves are mechanical stress waves propagating along the structures and guided by its boundaries. Lamb wave refers to guided wave propagates in plates with wavelength larger or of the order of the plate thickness [8]-[11]. In the last two decades, Lamb wave has been widely used for damage detection of plate-like structures [12]-[15]. When the wavelength of the guided wave is much smaller than the thickness of the structures, e.g. semi-infinite medium, guided wave becomes Rayleigh wave [16].

1.1 Damage Detection Using Rayleigh wave

Rayleigh wave is a type of surface wave that propagates along the surface of structures. The major portion of the energy of Rayleigh wave is concentrated along or near the surface of the structures, which means it can be used to detect surface or near-surface damages. In the literature, Rayleigh wave was employed to detect surface defects in concrete structures. Hevin *et al*. [17] employed the Rayleigh wave to detect surface crack depth in concrete. A numerical model was developed to provide better understanding of Rayleigh wave and crack geometry. Sun *et al*. [18] employed low-profile piezoceramic transducers for generating and sensing Rayleigh wave in concrete beams. They demonstrated that it is potential to monitor cracking and deterioration of concrete beams using Rayleigh wave. Aggelis *et al*. [19] demonstrated that Rayleigh wave is possible to be used for damage detection. They also correlated the wave parameters with crack depth to provide crack determination. Lee *et al*. [20] proposed an amplitude index to characterise the surface crack in concrete structures. They numerically and experimentally demonstrated the reliability of the proposed method.

For strengthening and repairing purpose, fibre reinforced polymer (FRP) has been widely used to retrofit concrete structures. The use of FRP has a number of advantages, such as ease of preparation and application, adjustable mechanical properties, and corrosion resistant etc. These advantages make the FRP become one of the most popular materials in retrofitting the concrete structures. However, debonding between the FRP and concrete interface is a serious problem, especially for long-term performance of the structures. Different conventional damage detection techniques were developed for detecting the debonding, such as visual inspection [21] and hammer tapping [22], infrared thermography [23] and acoustic emission technique [24], etc.

Rayleigh wave has been used to detect debonding in the FRP-retrofitted concrete structures. However, most of the existing studies only focused on linear Rayleigh wave. Sohn *et al.* [25] proposed a time-reversal approach using linear guided wave signal to detect the debonding in carbon fibre reinforced polymer (CFRP) strengthened reinforced concrete beams. The performance of the proposed approach was compared with electro-mechanical impedance method and infrared imaging technique. Mahmoud *et al.* [26] employed the linear surface wave to provide a nondestructive evaluation (NDE) of the concrete structures with externally bonded CFRP composites. Specimens under water-immersion aging at different temperatures were monitored over 12 weeks. They showed that the linear surface wave could be used to monitor the condition of the CFRP strengthened concrete structures. Mohseni and Ng [27] carried out a comprehensive study of linear Rayleigh wave propagation and scattering characteristics at debondings in FRP-retrofitted concrete structures. In their study, 3D scanning laser vibrometer was used to investigate the scattering characteristics of linear Rayleigh wave at the debonding. They also [28] proposed a technique using the time-of-flight information of linear Rayleigh wave to detect and locate the debonding. The results showed that the time-of-flight information of linear Rayleigh wave could accurately determine the existence and location of the debonding.

1.2 Nonlinear features for damage detection

Nonlinear features of guided wave have attracted increasing attention in recently years. Majority of studies focused on two aspects, understanding the behaviour of the nonlinear features and development of damage detection techniques using the nonlinear features. One of the most commonly used nonlinear features for damage detection is higher harmonics generation in response to single-frequency excitation. When guided wave interacts with the contact type damage, scattered waves are not only observed at excited fundamental frequency, but also at integral multiples of the fundamental frequency, i.e. higher harmonic frequencies, due to the effect of contact nonlinearity. Since the damage information exists at higher harmonic frequencies, which are separated from the excited fundamental frequency, it does not require reference data to extract the damage information for damage detection. Therefore, higher harmonic generation is potential to be used for reference-free damage detection. This can address challenges of using linear guided wave based damage detection techniques, such as temperature [29]- [32] and load dependence [33]-[35] issue of using the reference data.

Higher harmonics induced by contact nonlinearity have been used for detecting contact type of damage in thin-walled structures. A number of studies were carried out to provide numerical predictions and gain physical insights into the higher harmonics generation at different types of damages, such as fatigue crack [36],[37], delamination [38],[39], thermal fatigue [40], and material degradation [41] in thin-walled structures. These studies demonstrated that the higher harmonics generation could be used for damage detection and are more sensitive than linear feature of guided wave. Li *et al*. [40] used the second harmonic Lamb wave to detect thermal fatigue damage in composite laminates. They showed that the acoustic nonlinearity monotonically increase with respect to thermal fatigue cycles. They demonstrated that the second harmonic could be used to assess thermal fatigue damage with better performance than conventional linear feature of Lamb wave. Su *et al*. [42] compared the performance of the linear and nonlinear features of guided wave in detecting fatigue crack in metallic plates. The results show that the nonlinear feature outperforms their linear counterparts in term of damage detectability. Soleimanpour and Ng [43] employed the second harmonic generation of the fundamental anti-symmetrical mode of Lamb wave to detect and locate the delamination in laminated composite beams. The results show that the delamination can be detected and located using the time-of-flight information of the second harmonic wave. Yi *et al*.

[44] presents a numerical and experimental study of the second harmonic generation at fatigue cracks in aluminum plates. They studies provided physical insights into the second harmonic generation due to Lamb wave interaction with the fatigue cracks. They also extended the work to investigate the effect of crack opening and incident wave angle on second harmonic generation of Lamb waves [45].

For the development of using nonlinear Rayleigh wave, Kawashima *et al*. [46] presented a numerical and experimental study of nonlinear Rayleigh wave generated at surface cracks in aluminium. They showed that the second harmonic amplitude is more pronounced for low compressive stress applied to close the crack. Zhang *et al*. [47] showed that the higher harmonic generation of Rayleigh wave could be used to detect surface scratches in glass. They investigated the effect of the surface scratches in relation to the characteristics of the higher harmonic generation of Rayleigh wave. Yuan *et al*. [48] carried out a numerical study of higher harmonic generated due to Rayleigh wave interacting at cracks with different depths. They also analysed the coupling effect of clapping and slipping mechanisms for Rayleigh wave.

Different to the aforementioned developments, this study focuses on debonding detection for the FRP-retrofitted reinforced concrete structures. The second harmonic generation due to Rayleigh wave interaction with the debonding is used as the nonlinear feature to detect and locate the debonding. One of the advantages of the proposed technique is that it does not require the reference data, and hence, it has less influence by varying environmental condition. In addition the proposed method also provides a graphical representation of the damage, which not only pinpoints the location of the damage but also reconstructs a possible damage area. This provides quantitative information for engineers with the potential to assess the need for any required remedial work.

The paper is organised as follows. Section 2 presents the detail of the proposed damage detection method, in which the concept of contact nonlinearity is first introduced, and then the damage image reconstruction algorithm and the corresponding signal processing technique are described in details. Section 3 presents the experimental case studies. The experiment setup and FRP-retrofitted reinforced concrete specimens are first described, and then the calculation of group velocities and damage detection results are discussed in detail. Finally, conclusions are drawn in Section 4.

2 Damage detection technique using second harmonic Rayleigh wave generated by contact nonlinearity

2.1 Contact nonlinearity

Contact nonlinearity is a localised nonlinearity induced by contact defects, such as cracks, delamination and debonding. The characteristic feature of contact nonlinearity is a contacting interface, in which surface are initially either touching or in a very close proximity. Higher harmonic generation is due to the repetition of collision between the two surfaces caused by incident ultrasonic wave. Using a debonding at a pair of interfaces as an example to illustrate the concept, when the ultrasonic wave interacts with the debonding, clapping of the interfaces occurs due to the asymmetrical dynamics of the interface stiffness. Solodov *et al.* [49] proposed a theoretical formulation to model this phenomenon. In general, the contact nonlinearity is due to the stiffness asymmetry of near-surface strain across the interfaces. When the interface with the debonding is under compression, it is accompanied by weakening or rupture of the contact between the interface surfaces, and hence, the compression elasticity is higher than that when it is subjected to tensile stress. Based on this characteristic, a bi-modular area is created when the ultrasonic wave passes through the contact interfaces, and this can be model by a piece-wise stress-strain relation [49]. Higher harmonics are generated due to the change of the local stiffness at the debonding region.

These higher harmonics correlate the presence and characteristics of the debonding with measured wave signals, which contains not only the frequency of the input signal to the structures, but also its integral multiple frequencies. In this study, the second harmonic induced due to the Rayleigh wave interaction with the debonding is used to detect and locate the debonding in the CFRP-retrofitted reinforced concrete structures. The damage detection technique proposed in this study relies on the second harmonic Rayleigh wave, which is different to the excitation frequency of the input signal, and hence, it does not require the reference data to extract the damage information from the measured signal.

2.2 Debonding detection method using nonlinear Rayleigh wave

The proposed damage detection method determines the existence and location of the debonding based on second harmonic Rayleigh wave. A transducer network with N transducers is required to sequentially scan the targeted structures using Rayleigh wave. Each of the transducer can be used as both actuator and sensor to excite and measure the wave signals, respectively. In the sequential scan, when one of the transducers is used to excite the Rayleigh wave in the CFRP-retrofitted reinforced concrete structure, the rest of the transducers are used to measure the wave signals. This provides a total of $N(N-1)$ actuator/sensor signal paths.

Figure 1a shows a transducer network with four transducers, T_1, T_2, T_3 and T_4, which is used as an example to illustrate the proposed debonding detection method. In the sequential scan, the transducer T_1 is first used as the actuator to excite the Rayleigh wave, while the transducers T_2, T_3 and T_4 are used as the sensor to measure the wave signals. The incident Rayleigh wave propagates and reaches the debonding. When the incident Rayleigh wave interacts with the debonding, wave scattering occurs and the second harmonic of Rayleigh wave is also generated due to the contact nonlinearity at the debonding. Therefore, the signals measured by the transducers include the incident Rayleigh wave, the scattered waves from the debonding, which contain components at fundamental and second harmonic frequency, and also the wave reflected from the boundaries of the structure. This process is repeated N-1 times with transducer T_2, T_3 and T_4 being used as the actuator, respectively. Once the sequential scan process is completed, the measured signals are post-processed to determine the debonding location using the proposed damage detection method.

[Figure 1: a) Rayleigh wave propagation and scattering at debonding between CFRP and concrete interface, b) discretization of inspection area by image pixels]

The idea of the proposed damage detection method is to discretise the inspection area into image pixels as shown in Figure 1b. Without loss of generality, transducers i and j are used as an example to illustrated the damage detection algorithm. When Rayleigh wave interacts with the debonding, the second harmonic of Rayleigh wave is generated. Therefore, it is assumed that the wave propagation can be separated into two stages. In the first stage, the Rayleigh wave is generated from the transducer i at (x_i, y_i) and then propagate to the image pixel at (x,y). In the second stage, it is assumed that the image pixel is considered as the potential debonding location, and hence, the second stage considers the second harmonic of Rayleigh wave is generated at the debonding location (the image pixel being considered) and propagates to the transducer j at (x_j, y_j). Since the locations of the transducers and image pixels are known in advance before carrying out the damage inspection, the group velocity of Rayleigh wave at fundamental and second harmonic frequency can be obtained theoretically or measured experimentally. The arrival time of the second harmonic Rayleigh wave can be calculated by

$$T_{ij}(x,y) = \frac{\sqrt{(y-y_i)^2+(x-x_i)^2}}{c_{g,f}(\theta_i)} + \frac{\sqrt{(y_j-y)^2+(x_j-x)^2}}{c_{g,2f}(\theta_j)} \tag{1}$$

where $c_{g,f}$ and $c_{g,2f}$ are the group velocity of the Rayleigh wave at fundamental and second harmonic frequency, respectively. θ_i and θ_j are the Rayleigh wave propagation direction from transducer i to the image pixel and from the image pixel to the transducer j. The first and second term at the right-hand side of the Equation (1) is the arrival time of the fundamental frequency Rayleigh wave from the transducer i to the image pixel (x,y), and the second harmonic Rayleigh wave from the image pixel (x,y) to the transducer j, respectively.

Since the measured wave signal at transducer j contains both fundamental and second harmonic Rayleigh wave, a short-time Fourier transform (STFT) is used to extract the second harmonic Rayleigh wave and it is defined as

$$S_{ij}(t,f) = \sum_{m=-\infty}^{\infty} u_{ij}(m) w(m-t) e^{-j2\pi f m} \tag{2}$$

where u_{ij} is the measured signal using the transducer i as the actuator and transducer j as the sensor. $w(m)$ is the window function and *m* is the window interval centered around zero. In this study, the window interval is carefully chosen such that sufficient details of both time and frequency information of the measured signal could be retained. *f* is the frequency in Hertz.

In the proposed method, a cross-correlation analysis between the incident pulse at fundamental frequency input to transducer *i* and second harmonic of Rayleigh wave measured at transducer *j* is used to determine the time shift for describing the source location of the second harmonic Rayleigh wave. As the second harmonic is induced due to the contact nonlinearity at debonding, it can be used to determine the debonding location. Figure 2 shows a schematic diagram of the incident wave and the measured nonlinear Rayleigh wave in the proposed debonding detection technique. The incident Rayleigh wave only contains components excited at fundamental frequency.

[Figure 2: Schematic diagram of the proposed damage debonding method and signal processing]

The incident Raleigh wave propagates and interacts with the debonding. The second harmonic Rayleigh wave is then induced due to the contact nonlinearity at the debonding. Therefore, the measured signal by the transducer contains components at both excited fundamental frequency and second harmonic frequency as shown in Figure 2. With the information of the incident wave components at the fundamental frequency and damage information at the second harmonic frequency, the cross-correlation C_{ij} is defined as

$$C_{ij}(t) = \int_0^T S_F(\tau, f_c) S_{ij}(\tau + t, 2f_c) d\tau \tag{3}$$

where S_F is the STFT transformed incident pulse. S_{ij} is the STFT transformed signal measured by transducer *j* while transducer *i* is used as actuator. *T* is the duration of the measured signal. f_c and $2f_c$ is the central frequency of the excitation signal and the corresponding second harmonic frequency, respectively.

In the sequential scan, there are *N*(*N*-1) actuator/sensor paths. For each actuator/sensor path, the magnitude of a set of image pixels in the inspection area can be calculated and the magnitude of the cross-correlation at the possible damage location has the largest value. To determine the debonding location, the image indicating the possible debonding location can be obtained by superimposing the power flux of all actuator/sensor path images as [50]

$$I(x,y) = \sum_{i=1}^{N} \sum_{j \neq i}^{N} \kappa_{ij} C_{ij} \left[T_{ij}(x,y)\right]^2 \tag{4}$$

where κ_{ij} is the weighting factor used to take into account the varying sensitivity of each actuator/sensor path image. In this study, it is assumed to be uniform aperture weighting, i.e. equals to unity.

3 Experimental studies

3.1 Specimens and experiment setup

Two specimens of CFRP-retrofitted reinforced concrete block are used to verify the proposed debonding detection method. The dimensions of the concrete blocks are 300mm×600mm×300mm (W×L×H). The Young's modulus and density of the concrete is 26.8GPa and 2350kg/m^3, respectively. The maximum size of aggregate is 10mm. Four 16mm diameter rebars are installed at four corners of the cross-section of the concrete block as shown in Figure 1a and the concrete cover is 6mm. Four layers of 300mm×600mm unidirectional CFRP with stacking sequence of $[0]_4$ were bonded on the concrete surface using a hand lay-up method. Each layer of fibre is saturated by BASF MasterBrace 4500 epoxy resin. Four 2mm thick and 10mm diameter circular piezoceramic transducers (Ferroperm Pz27) were used to actuate and sense Rayleigh wave. The transducers were bonded to the surface of the CFRP and they are located at T_1 (x_1 = 160mm, y_1 = 70mm), T_2 (x_2 = 360mm, y_2 = 70mm), T_3 (x_3 = 360mm, y_3 = 220mm), and T_4 (x_4 = 160mm, y_4 = 220mm). The excitation signal is a 95kHz, 15-cycle sinusoidal tone burst modulated by a Hanning window. The wavelength of the incident Rayleigh wave is around 22mm.

Case 1 considers the specimen has a 60mm×60mm debonding between the CFRP and concrete interface. The centre of the debonding is located at x = 300mm and y = 150mm based on the Cartesian coordinate shown in Figure 3. In Case 2, the specimen has a 40mm×300mm debonding, which is across the whole width of the concrete block and located between *x* = 280mm and *x* = 320mm. The debonding was created by placing a Mylar sheet on the concrete surface before applying the first fibre layer.

[Figure 3: Schematic diagram of the CRFP-retrofitted concrete block and the layout of the surface-mounted transducer network (top view), a) 60mm×60mm debonding, and b) 40mm×300mm debonding]

Figure 4 shows the experiment setup used in this study. A PC-controlled NI PXI-5412 waveform generator was used to generate the excitation signal. The amplitude of the generated signal was then amplified by five times to 50V (peak-to-peak) using a KROHN-HITE 7500 amplifier. The signals measured by the piezoceramic transducers were recorded by NI PXI-5105 digitizer and the data was then sent to computer for analysis. The sampling frequency was set to 10.24 MHz and the signals were averaged 5000 times to improve the signal-to-noise ratio.

[Figure 4: Schematic diagram of the experiment setup used in the proposed debonding detection technique]

3.2 Theoretically calculated and experimentally measured group velocities

The CFRP-retrofitted reinforced concrete structure considered in this study is anisotropic material. The group velocities of Rayleigh wave at different propagation directions are different. Therefore, the proposed debonding detection technique requires the information of the group velocity to detect and locate the debonding in the CFRP-retrofitted reinforced concrete structure. As mentioned in Section 2.2, the group velocity can be obtained theoretically or measured experimentally. This section provides a comparison of the theoretically calculated and experimentally measured group velocities.

The theoretical values of the group velocities were calculated using DISPERSE. For the experimentally measured group velocities, one of the transducers was used to excite the Rayleigh wave and the Polytec PSV-400 laser Doppler vibrometer [51] was used to measure the Rayleigh wave signals. The equipment used for the group velocity measurement is shown in Figure 5. In general, most of the equipment is the same as those in Figure 4, except the data acquisition and the laser vibrometer. The measurements were carried out at every 10°. For each propagation direction, five measurement points were taken at the same distance away to each other. The time-of-flight of the Rayleigh wave at each propagation direction was estimated using the signal envelope obtained from the Hilbert transform. Based on the time-of-flight and distance between two of the measurement points, the group velocity can be estimated. The averaged group velocity at each propagation direction is then used in the proposed damage detection technique to detect and locate the debonding.

[Figure 5: Laser vibrometer for group velocity measurement]

As an example, Figure 6 shows the angular dependence of the theoretically calculated and experimentally measured group velocity at fundamental frequency (95kHz) for Rayleigh wave propagation in different directions on the CFRP-retrofitted reinforced concrete structure. The results show that there is good agreement between the theoretically calculated and experimentally measured group velocities. In this study, the theoretically calculated group velocities are used in the proposed debonding detection technique to detect and locate the debonding in the CFRP-retrofitted reinforced concrete specimen in the experimental study. Figure 7 shows the theoretically calculated angular dependence of the group velocity of the Rayleigh wave at second harmonic frequency (190kHz).

[Figure 6: Angular dependence of group velocity at 95kHz in ms^{-1} for the CFRP-retrofitted concrete structures (cirlces: DISPERSE data, crosses: experimental data)]

[Figure 7: Angular dependence of group velocity at 190kHz in ms^{-1} for the CFRP-retrofitted

concrete structures calculated by DISPERSE]

3.3 Results and discussion

Figure 8 shows the data measured from signal path T_1-T_4 for the specimen in Case 1, in which the transducer T_1 is used as actuator to excite Rayleigh wave while the transducer T_4 is used as sensor to measure the scattered wave signals. It is used as an example to illustrate and explain the wave packages in the measured signal. As mentioned in Section 3.1, the specimen has a 60mm×60mm debonding. As shown in Figure 8, the signal contains a number of wave packages. The first wave package is the incident wave, which propagates directly from the transducer T_1 to T_4. The second wave package is the scattered wave from the debonding. As shown in Figure 3a, signal path from the transducer T_1 to the debonding, and then transducer T_4 is longer than the direct signal path from the transducer T_1 to T_4. Therefore, the scattered wave arrives after the incident wave. The last wave package is the waves reflected from the boundaries and they are overlapped together as shown in Figure 8.

[Figure 8: Measured data of signal path T_1-T_4 with debonding size 60mm × 60mm]

As shown in Figure 8, the scattered wave package is partially mixed with the incident wave and boundary reflections. For damage detection technique based on the linear feature, it is essential to extract the scattered wave signal for damage detection using baseline data. Different to the linear feature, the second harmonic Rayleigh wave can be extracted using the time-frequency analysis without the baseline data. Figure 9 shows the corresponding time-frequency energy spectrum of the signal transformed using the STFT described in Section 2.2. The figure shows that the time-frequency spectrum contains not only the signal components at the excited fundamental frequency (95kHz), but also the second harmonic frequency (190kHz). Figure 10 shows the corresponding normalised spectral amplitude at the excited fundamental frequency and second harmonic frequency. The second harmonic wave is generated due to the contact nonlinearity at the debonding. When the incident wave reaches and interacts with the debonding, the second harmonic wave is generated due to the contact nonlinearity. The second harmonic wave propagates and is then measured by the transducer T_4. The results show that the arrival time is consistent with the scattered wave from the debonding. Since the second harmonic wave exists at the second harmonic frequency, it does not require the baseline data to extract the damage information.

[Figure 9: Energy density spectrum in time-frequency domain for the data of signal path T_1-T_4 with debonding size 60mm × 60mm]

[Figure 10: Normalised specral amplitude of signal path T_1-T_4 at fundamental frequency and second harmonic frequency for debonding size 60mm × 60mm]

Once the sequential scan process is completed, the measured signals are then processed using the STFT to extract the spectral amplitude at the second harmonic frequency. Using the data obtained at from signal path T_1-T_4 as an example, it is $S_{14}(t, 190\text{kHz})$. With this information and the spectral amplitude of the incident wave at the excited fundamental frequency $S_F(t, 95\text{kHz})$, an actuator/sensor path image for T_1-T_4 is obtained and shown in Figure 11. The image indicates the feasible debonding location based on the data measured by signal path T_1-T_4. The pixel size used in this study is 1mm. The white dashed lines in the figure indicate the actual debonding location, size and shape. Using Equation 4, the reconstructed image for indicating the debonding location can be obtained by superimposing all the actuator/sensor path images. Figure 12a shows the reconstructed image for Case 1. An arbitrary threshold value is used to filter out minor intensity peaks to provide a robust image for determining the location of the debonding.

[Figure 11: Typical image of actuator/sensor signal paths T_1-T_4 for debonding size 60mm × 60mm]

As an example, Figure 12b shows a binary image created from Figure 12a using threshold value is 95%. The binary image is obtained by only accounting for image pixels whose intensity is larger than an arbitrary threshold value. The centroid of the binary image, which is calculated by the ratio of the first- and zeroth-order spatial moments of the binary image, can be used to determine the predicted debonding location [52]. Based on centroid of the binary image, the predicted centroid location of the debonding is at x_p = 321.30mm and y_p = 170.97mm and it is indicated by a cross marker in Figure 12b. The predicted debonding location is within the true debonding area x_d = 300±30mm and y_d = 150±30mm. A debonding locating error is defined as $E=\sqrt{(x_p-x_d)^2+(y_p-y_d)^2}$ to quantify the error of the predicted debonding location. For threshold value 95%, the debonding locating error E = 29.89mm. In this study, the effect of the threshold values from 80% to 95% with steps of 5% is investigated. Table 1 summarizes the debonding detection results and debonding locating error using different threshold values. In general, the performances of the threshold values from 80% to 95% are similar.

[Figure 12: a) Debonding location image and b) corresponding binary image for Case 1 with debonding size 60mm × 60mm (Circles: piezoceramic transducers, dashed line: actual debonding location and size, cross: predicted debonding location based on the centroid of the binary image)]

[Table 1: Summary of all cases and debonding detection results using different threshold values]

Different to Case 1, Case 2 considers a debonding, which is across the whole width of the concrete block. The reconstructed image for Case 2 is shown in Figure 13a. As an example, the corresponding binary image with threshold value is 95% is shown in Figure 13b. The same as Case 1, dashed lines are used to indicate the actual debonding location, size and shape. The predicted damage location for Case 2 is at x_p = 318.76mm ad y_p = 141.26mm, and it is indicated by a cross marker in Figure 13b. The same as Case 1, the effect of different values are also investigated and the predicted debonding results are summarized in Table 1. Overall, the predicted debonding locations for Cases 1 and 2 are both within the actual debonding region. The results demonstrate that the proposed damage detection technique is able to provide a reliable prediction of the debonding location in the CFRP-retrofitted reinforced concrete structures.

[Figure 13: a) Debonding location image and b) corresponding binary image for Case 2 with debonding size 40mm × 300mm (Circles: piezoceramic transducers, dashed line: actual debonding location and size)]

4 Conclusions

This paper has presented a debonding detection technique using nonlinear Rayleigh wave for CFRP-retrofitted reinforced concrete structures. The nonlinear feature employed in the proposed debonding detection technique is second harmonic generated due to contact nonlinearity at the debonding. The proposed debonding detection technique is a reference-free approach, which could detect and locate the debonding between the CRFP and concrete interfaces.

In this study, the proposed debonding detection technique has been verified using experimental results. The results show that the reconstructed binary damage image is able to accurately predict the debonding location. One of the advantages of the proposed debonding detection technique is that it only requires a few transducers to locate the debonding in a reasonable size of inspection area. Since the proposed technique only involves computational efficient algorithms, such as signal processing technique using STFT, and simple cross-correlation analysis, it has the potential to achieve real-time in-situ debonding detection if it is used together with a multiplexed data acquisition system, which allows simultaneous measurement of signals from different transducers and sequential excitation of Rayleigh wave at each transducer. In summary, the study has shown the potential of applying the proposed debonding detection technique for in-situ structural health monitoring.

5 Acknowledgement

The work was supported by the Australian Research Council under grant number DE130100261. The support is greatly appreciated.

6 References

[1] C.S. Wang, F. Wu, F.K. Chang, Structural health monitoring from fiber-reinforced composites to steel-reinforced concrete, Smart Mater. Struct. 10 (2001) 548-522.

[2] V. Giurgiutiu, A. Cuc, Embedded non-destructive evaluation for structural health monitoring, damage detection, and failure prevention, Shock Vib. Dig. 37 (2005) 83-105.

[3] F. N. Catbas, M. Gul, J.L. Burkett, Conceptual damage-sensitive features for structural health monitoring: Laboratory and field demonstrations, Mech. Syst. Sig. Process. 22 (2008) 1650-1669.

[4] S. He, C.T. Ng, Guided wave-based identification of multiple cracks in beams using a Bayesian approach, Mech. Syst. Sig. Process. 84(Part A) (2017) 324-345.

[5] P. Malinowski, T. Wandowski, W. Ostachowicz, Damage detection potential of a triangular piezoelectric configuration, Mech. Syst. Sig. Process. 25 (2011) 2722-2732.

[6] Y.K. An, H. Sohn, Integrated impedance and guided wave based damage detection, Mech. Syst. Sig. Process. 28 (2012) 50-62

[7] A. Bagheri, K. Li, P. Rizzo, Reference-free damage detection by means of wavelet transform and empirical mode decomposition applied to Lamb waves, J. Intelligent Mater. Syst. Struct. 24 (2013) 194-208.

[8] P. Cawley, D. Alleyne, The use of Lamb waves for the long range inspection of large structures, Ultrasonics, 34 (1996) 287-290.

[9] V. Giurgiutiu, Structural health monitoring: with piezoelectric wafer active sensor, Academic Press, 2007.

[10] J.L. Rose, Ultrasonic guided waves in solid media, Cambridge University Press, 2014.

[11] C.T. Ng, On accuracy of analytical modeling of Lamb wave scattering at delaminations in multilayered isotropic plates, Inter. J. Struct. Stab. Dyn. 15 (2015) 1540010.

[12] E.B. Flynn, M.D. Todd, A.J. Croxford, B.W. Drinkwater, P.D. Wilcox, Enhanced detection through low-order stochastic modeling for guided-wave structural health monitoring, Struct. Health Monitor. 11 (2012) 149-160.

[13] H. Cho, C.J. Lissenden, Structural health monitoring of fatigue crack growth in plate structures with ultrasonic guided waves, Struct. Health Monitor. 11 (2012) 393-404.

[14] S. He, C.T. Ng, A probabilistic approach for quantitative identification of multiple delaminations in laminated composite beams using guided wave, Eng. Struct. 127 (2016) 602-614.

[15] G.T. Pudipeddi, C.T. Ng, A. Kotousov, Effect of central and non-central frequency components on the quality of damage imaging, J. Civil Struct. Health Monitor. (2018) DOI:

10.1007/s13349-017-0258-z

[16] B.W. Ti, W.D. O'Brien, Measurements of coupled Rayleigh wave propagation in an elastic plate, J. Acoust. Soc. Am. 102 (1997) 1528-1531.

[17] G. Hevin, O. Abraham, H.A. Pedersen, M. Campillo, Characterisation of surface cracks with Rayleigh waves: a numerical model, NDT&E Inter. 31 (1998) 289-297.

[18] M. Sun, W.J. Staszewski, R.N. Swamy, Z. Li, Application of low-profile piezoceramic transducers for health monitoring of concrete structures, NDT&E Inter. 41 (2008) 589-595.

[19] D.G. Aggelis, T. Shiotani, D. Polyzos, Characterization of surface crack depth and repair evaluation using Rayleigh waves, Cement & Concrete Compos. 31 (2009) 77-83.

[20] F.W. Lee, K.S. Lim, H.K. Chai, Determination and extraction of Rayleigh-waves for concrete cracks characterization based on matched filtering of center of energy, J. Sound Vib. 363 (2016) 303-315.

[21] I. Nishizaki, S. Meiarashi, Long-term deterioration of GFRP in water and moist environment, J. Compos. Constr. 6 (2002) 21-27.

[22] G.A. Washer, S. Alampalli, Nondestructive evaluation methods for composite materials: General overview, visual inspection, and microwave methods, The International Handbook of FRP Composites in Civil Engineering, CRC Press, 2014.

[23] J.R. Brown, H.R. Hamilton, Quantitative infrared thermography inspection for FRP applied to concrete using single pixel analysis, Constr. Build. Mater. 38 (2013) 1292-1302.

[24] A. Mirmiran, M. Shahawy, H.E. Echary, Acoustic emission monitoring of hybrid FRP-concrete columns, J. Eng. Mech. 125 (1999) 899-905.

[25] H. Sohn, S.D. Kim, C.W. In, K.E. Cronin, K. Harries, Debonding monitoring of CFRP strengthened RC beams suing active sensing and infrared imaging, Smart Struct. Syst. 4 (2008) 391-406.

[26] A.M. Mahmoud, H.H. Ammar, O.M. Mukdadi, I. Ray, F.S. Imani, A. Chen, J.F. Davalos, Non-destructive ultrasonic evaluation of CRFP-concrete specimens subjected to accelerated aging conditions, NDT&E Inter. 43 (2010) 635-641.

[27] H. Mohseni, C.T. Ng, Rayleigh wave propagation and scattering characteristics at debondings in fibre-reinforced polymer-retrofitted concrete structures, Struct. Health Monitor. (2018) https://doi.org/10.1177/1475921718754371

[28] H. Mohseni, C.T. Ng, Rayleigh wave for detecting debonding in FRP-retrofitted concrete structures using piezoelectric transducers, Comp. Concrete 20 (2017) 583-593.

[29] G. Konstantinidis, B.W. Drinkwater, P.D. Wilcox, The temperature stability of guided wave structural health monitoring systems, Smart Mater. Struct. 15 (2006) 67-76.

[30] A. Marzani, S. Salamone, Numerical prediction and experimental verification of temperature effect on plate waves generated and received by piezoceramic sensors. Mech. Syst. Sig. Process. 30 (2012) 204-217.

[31] P. Aryan, A. Kotousov, C.T. Ng, S. Wildy, Reconstruction of baseline time-trace under changing environmental and operational condition, Smart Mater. Struct. 25 (2016) 035018.

[32] P. Aryan, A. Kotousov, C.T. Ng, B. Cazzolato, A model-based method for damage detection

with guided waves. Struct. Contr. Health Monitor. 24 (2017) e1884.

[33] F. Chen, P.D. Wilcox, The effect of load on guided wave propagation, Ultrasonics, 47 (2007) 111-122.

[34] M. Mohabuth, A. Kotousov, C.T. Ng, Effect of uniaxial stress on the propagation of higher-order Lamb wave modes, Int. J. Non-linear Mech. 86 (2016) 104-111.

[35] M. Mohabuth, A. Kotousov, C.T. Ng, L.R.F. Rose, Implication of changing loading conditions on structural health monitoring utilizing guided waves, Smart Mater. Struct. 27 (2018) 025003.

[36] Y. Shen, V. Giurgiutiu, Predictive modeling of nonlinear wave propagation of structural health monitoring with piezoelectric wafer active sensor, J. Intell. Mater. Syst. Struct. 25 (2014) 506-520.

[37] S. He, C.T. Ng, Modelling and analysis of nonlinear guided waves interaction at a breathing crack using time-domain spectral finite element method, Smart Mater. Struct. 26 (2017) 085002.

[38] N.P. Yelve, M. Mitra, P.M. Mujumdar, Detection of delamination in composite using Lamb wave based nonlinear method, Comput. Struct. 159 (2017) 257-266.

[39] R. Soleimanpour, C.T. Ng, C.H. Wang, Higher harmonic generation of guided waves at delaminations in laminated composite beams, Struct. Health Monitor. 16 (2017) 400-417.

[40] W. Li, Y. Cho, J.D. Achenbach, Detection of thermal fatigue in composites by second harmonic Lamb waves, Smart Mater. Struct. 21 (2012) 085019.

[41] N. Rauter, R. Lammering, T. Kuhnrich, On the detection of fatigue damage in composites by use of second harmonic guided waves, Comp. Struct. 152 (2016) 247-258.

[42] Z. Su, C. Zhou, M. Hong, L. Cheng, Q. Wang, X. Qing, Acousto-ultrasonics-based fatigue damage characterization: Linear versus nonlinear signal features, Mech. Syst. Sig. Process. 45 (2014) 225-239.

[43] R. Soleimanpour, C.T. Ng, Locating delmainations in laminated composite beams using nonlinear guided waves, Eng. Struct. 131 (2017) 207-219.

[44] Y. Yang, C.T. Ng, A. Kotousov, H. Sohn, H.J. Lim, Second harmonic generation of fatigue cracks by low-frequency Lamb waves: Experimental and numerical studies, Mech. Syst. Sig. Process. 99 (2018) 760-773.

[45] Y. Yang, C.T. Ng, A. Kotousov, Influence of crack opening and incident wave angle on second harmonic generation of Lamb waves, Smart Mater. Struct. 27 (2018) 055013.

[46] K. Kawashima, R. Omote, T. Ito, H. Fujita, T. Shima, Nonlinear acoustic response through minutes surface cracks: FEM simulation and experimentation, Ultrasonics, 40 (2002) 611-615.

[47] J. Zhang, F.Z. Xuan, F. Yang, Effect of surface scratches on the characteristics of nonlinear Rayleigh surface waves in glass, J. Non-Crystalline Solids, 378 (2013) 101-105.

[48] M. Yuan, J. Zhang, S.J. Song, H.J. Kim, Numerical simulation of Rayleigh wave interaction with surface closed cracks under external pressure, Wave Motion, 57 (2015) 143-153.

[49] I.Y. Solodov, N. Krohn, G. Busse, CAN: an example of nonclassical acoustic nonlinearity in solids, Ultrasonics 40 (2002) 621-625.

[50] C.T. Ng, M. Veidt, A Lamb-wave based technique for damage detection in composite

laminates, Smart Mater. Struct. 18 (2009) 074006.

[51] P. Aryan, A. Kotousov, C.T. Ng, B.S. Cazzolato, A baseline-free and non-contact method for detection and imaging of structural damage using 3D laser vibrometry, Struct. Contr. Health Monitor. 24 (2017) e1894.

[52] W.K. Pratt, Digital Image Processing, Wiley, 1991.

Figure List

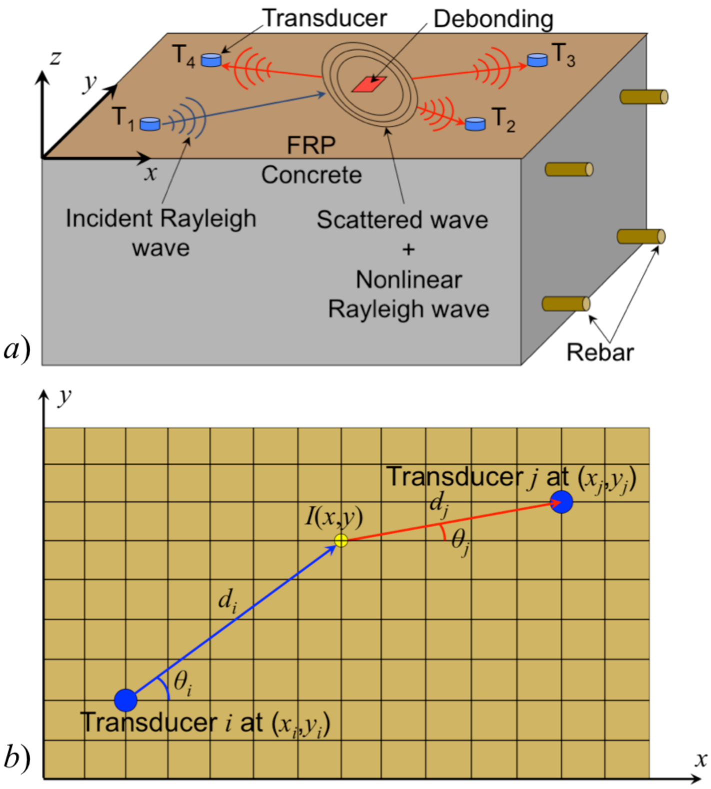

Figure 1: a) Rayleigh wave propagation and scattering at debonding between CFRP and concrete interface, b) discretization of inspection area by image pixels

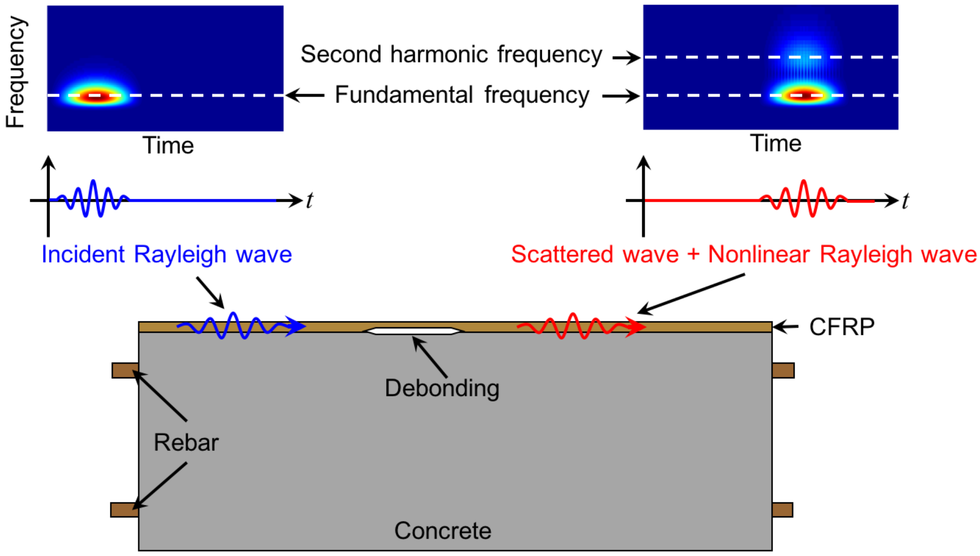

Figure 2: Schematic diagram of the proposed damage debonding method and signal processing

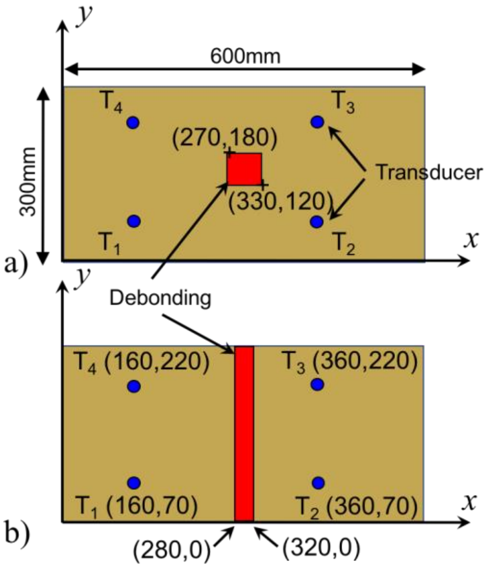

Figure 3: Schematic diagram of the CRFP-retrofitted concrete block and the layout of the surface-mounted transducer network (top view), a) 60mm×60mm debonding, and b) 40mm×300mm debonding

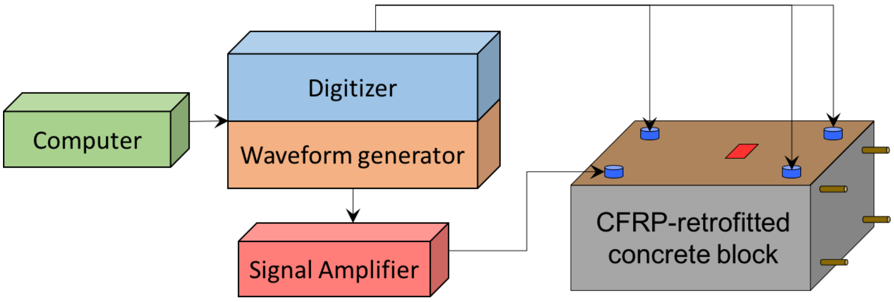

Figure 4: Schematic diagram of the experiment setup used in the proposed debonding detection technique

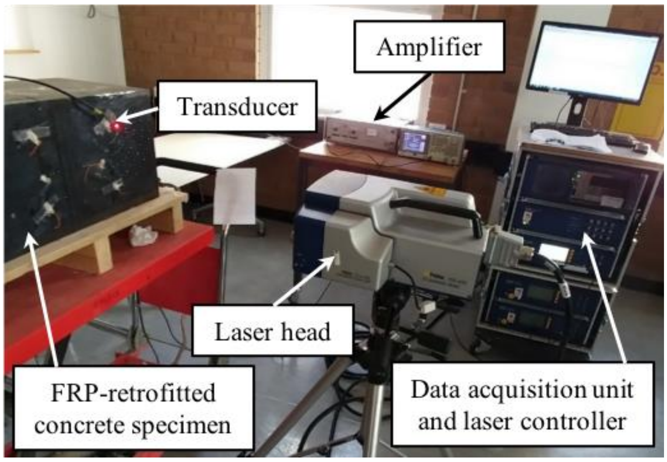

Figure 5: Laser vibrometer for group velocity measurement

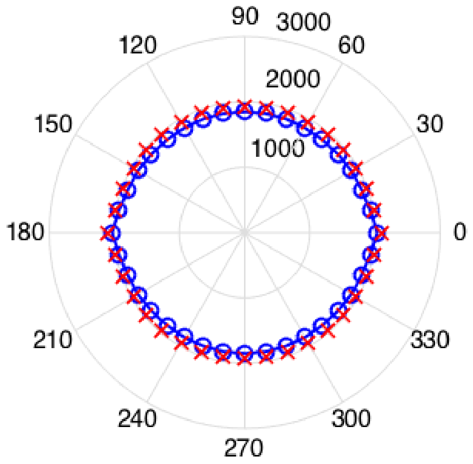

Figure 6: Angular dependence of group velocity at 95kHz in ms^{-1} for the CFRP-retrofitted concrete structures (cirlces: DISPERSE data, crosses: experimental data)

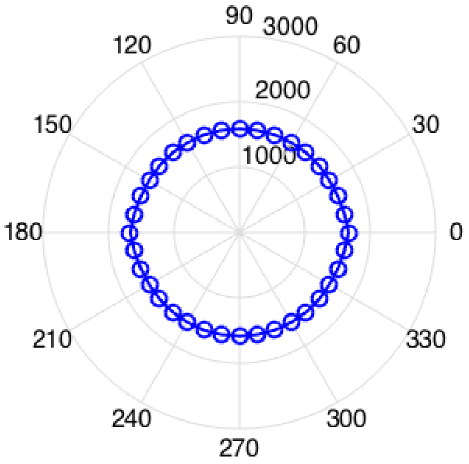

Figure 7: Angular dependence of group velocity at 190kHz in ms^{-1} for the CFRP-retrofitted concrete structures calculated by DISPERSE

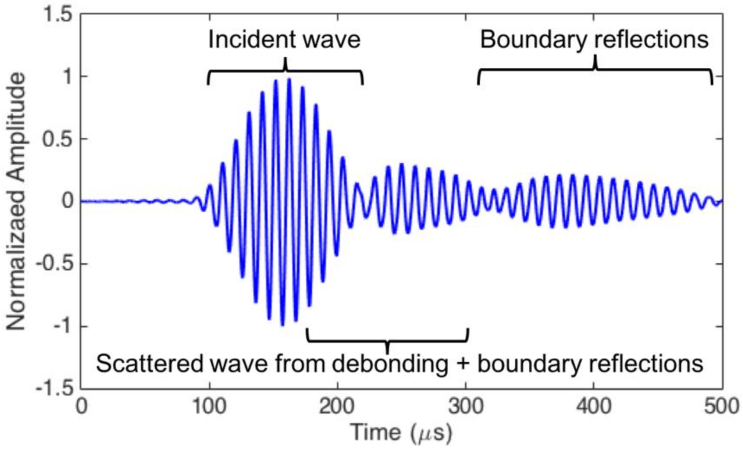

Figure 8: Measured data of signal path T_1-T_4 with debonding size 60mm × 60mm

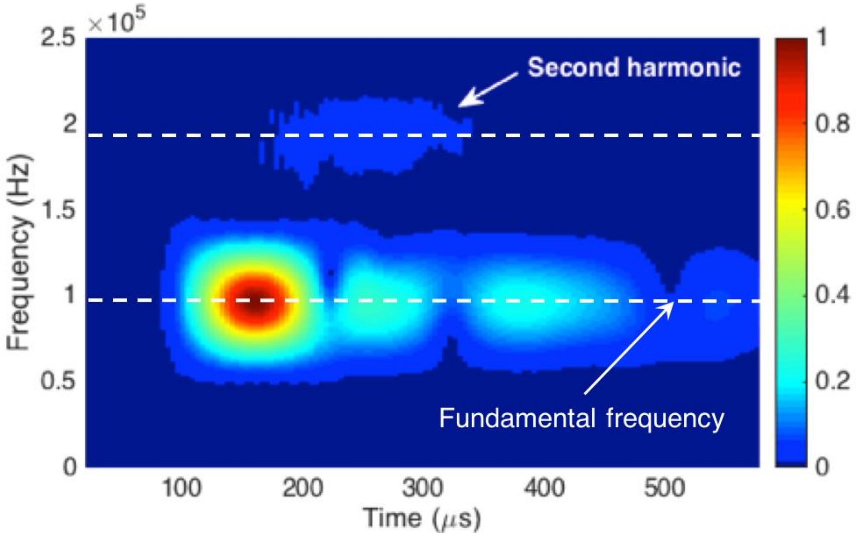

Figure 9: Energy density spectrum in time-frequency domain for the data of signal path T_1-T_4 with debonding size 60mm × 60mm

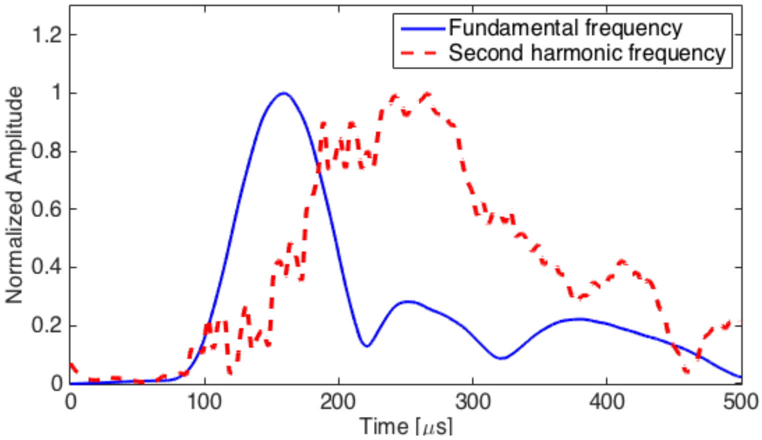

Figure 10: Normalised specral amplitude of signal path T_1-T_4 at fundamental frequency and second harmonic frequency for debonding size 60mm × 60mm

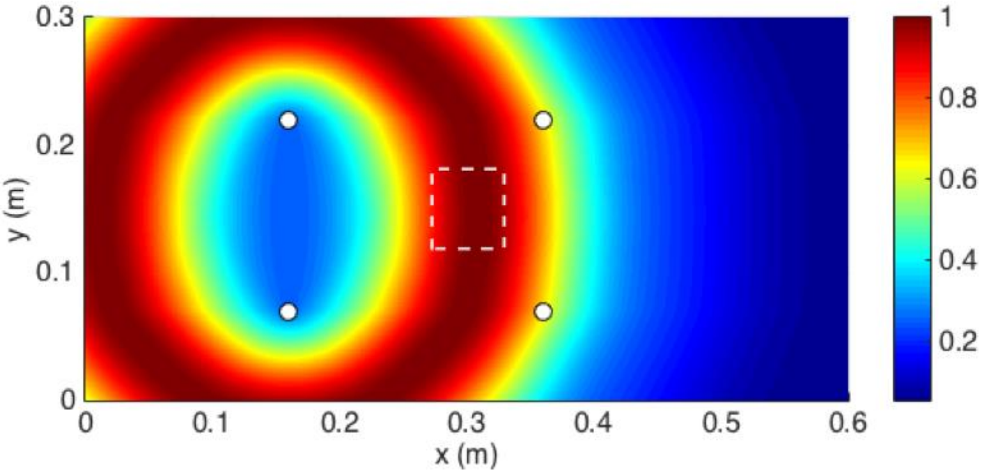

Figure 11: Typical image of actuator/sensor signal paths T_1-T_4 for debonding size 60mm × 60mm

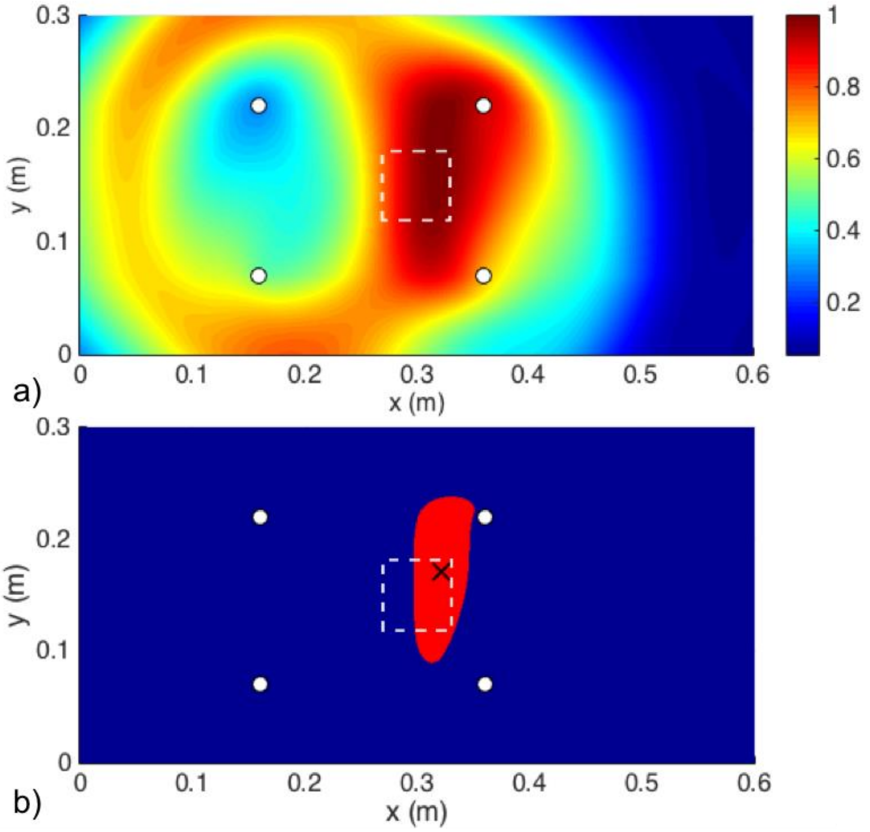

Figure 12: a) Debonding location image and b) corresponding binary image for Case 1 with debonding size 60mm × 60mm (Circles: piezoceramic transducers, dashed line: actual debonding location and size, cross: predicted debonding location based on the centroid of the binary image)

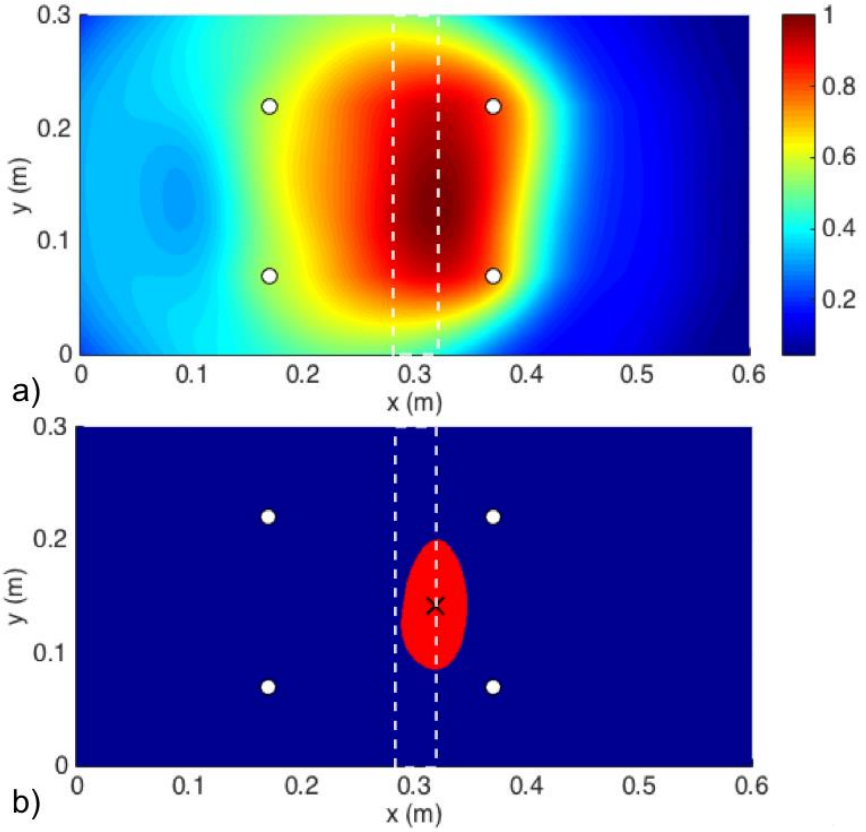

Figure 13: a) Debonding location image and b) corresponding binary image for Case 2 with debonding size 40mm × 300mm (Circles: piezoceramic transducers, dashed line: actual debonding location and size)

Table List

Table 1: Summary of all cases and debonding detection results using different threshold values

Case	True debonding centroid (mm)	Threshold value (%)	Predicted debonding location (mm)	Debonding locating error E (mm)
Case 1 (60mm×60mm debonding)	$x_d = 300\pm30$ $y_d = 150\pm30$	80	$x_p = 324.85$ $y_p = 165.80$	29.45
		85	$x_p = 324.92$ $y_p = 167.01$	30.17
		90	$x_p = 323.52$ $y_p = 168.04$	29.64
		95	$x_p = 321.30$ $y_p = 170.97$	29.89
Case 2 (40mm×300mm debonding)	$x_d = 300\pm20$ $y_d = 150\pm150$	80	$x_p = 311.79$ $y_p = 152.41$	12.04
		85	$x_p = 315.08$ $y_p = 150.38$	15.08
		90	$x_p = 317.37$ $y_p = 147.36$	17.57
		95	$x_p = 318.76$ $y_p = 141.26$	20.70